

Compressive Deconvolution Methods of Higher-Order- Aberrated Optical Systems

Saketh Malyala



Electrical Engineering and Computer Sciences
University of California, Berkeley

Technical Report No. UCB/EECS-2024-151

<http://www2.eecs.berkeley.edu/Pubs/TechRpts/2024/EECS-2024-151.html>

August 1, 2024

Copyright © 2024, by the author(s).
All rights reserved.

Permission to make digital or hard copies of all or part of this work for personal or classroom use is granted without fee provided that copies are not made or distributed for profit or commercial advantage and that copies bear this notice and the full citation on the first page. To copy otherwise, to republish, to post on servers or to redistribute to lists, requires prior specific permission.

Acknowledgement

I would like to thank Professor Brian Barsky for mentoring me through my four semesters in this group and encouraging me to explore uncharted territory. I am indebted to Joshua Chen, who has guided me through our research group's advances in compressive deconvolution. I would further like to acknowledge Matthew Fogel for assisting with data collection and debugging, as well as providing much needed documentation in our repositories to facilitate future research. I'd also like to mention, Siyu Zhang, who led me during my first semester on the vision correcting display project. Finally, I am extremely grateful to Professor Austin Roorda for reviewing this work as a second reader.

Masters Report

Compressive Deconvolution Methods of Higher-Order-Aberrated Optical Systems

by Saketh Malyala

Research Project

Submitted to the Department of Electrical Engineering and Computer Sciences,
University of California at Berkeley, in partial satisfaction of the requirements for the
degree of **Master of Science, Plan II.**

Approval for the Report and Comprehensive Examination:

Committee:

Brian A. Barsky

Professor Brian Barsky
Research Advisor

31 July 2024

(Date)

* * * * *

Austin Roorda

Professor Austin Roorda
Second Reader

July 31, 2024

(Date)

Abstract

Compressive Deconvolution Methods of Higher-Order-Aberrated Optical Systems

by

Saketh Malyala

Master of Science in Electrical Engineering and Computer Sciences in Mathematics

University of California, Berkeley

Professor Brian Barsky, Chair

A vast number of people around the world are affected by optical aberrations and require corrective lenses to see properly. Computational vision correction is an emerging solution to this problem. Vision correcting displays compute and display an image on a screen, such that a user can look at the screen unaided and see a focused picture. This work extends existing frameworks for compressive deconvolution based approaches to the vision correction problem, in order to accommodate higher order aberrations that are not correctable by traditional glasses or lenses. We explored a wavefront based approach for modeling generally aberrated optical systems and how the presence of higher order aberrations affects existing solutions. We modified the compressive deconvolution algorithm to accommodate the most common higher order aberrations. We examined tradeoffs between performance and algorithmic efficiency for these techniques. The results show that the forms of blurring caused by higher order aberrations require more expensive corrections to achieve satisfactory output quality.

To my family and friends

Thank you for challenging me, supporting me, and encouraging me to be my best.

Contents

Contents	ii
List of Figures	iv
List of Tables	v
1 Background	1
1.1 Introduction	1
1.2 The Eye	1
1.3 Problem Statement	3
2 Related Work	4
2.1 VCD	4
2.2 Light Field Displays	4
2.3 Light Field Display Algorithms for Vision Correction	5
3 Compressed Sensing Approaches to Image Construction	8
3.1 Sampling Problem	8
3.2 Compressed Sensing	9
3.3 Compressive Deconvolution Objective	10
4 Simulating Higher Order Aberrations	11
4.1 Ray-Tracing Model for Unaberrated Systems	11
4.2 Zernike Polynomials	13
5 Evaluation and Results	16
5.1 Display, User, and Model Parameters	16
5.2 Aberration Parameters	17
5.3 Selected Images for Vertically Oriented Zernike Modes of Aberration	17
5.4 Results	27
6 Future Work	29

7 Conclusion

30

Bibliography

31

List of Figures

1.1	The eye focuses light through the cornea and lens onto the retina. The retinal image is transmitted to the brain through the optic nerve.	2
1.2	Multiple light rays originate from each point on the tree, are refracted by the lens, and converge on the retina.	3
2.1	Pinhole arrays placed over pixel screens allow narrow, directional light rays to pass through.	5
2.2	Light field displays can be used to create 3D effects by using directional light rays that simulate depth.	6
4.1	Zernike polynomials form a set of orthonormal waveforms that are useful for describing visual aberrations.	14
4.2	The wavefront aberration polynomial describes the optical path difference between the wavefront and an unaberrated, reference spherical wave front.	15
5.1	Graphs comparing root-mean-square coma aberration and PSNR/SSIM quality metrics for corrected and uncorrected simulated retinal images.	20
5.2	Graphs comparing root-mean-square trefoil aberration and PSNR/SSIM quality metrics for corrected and uncorrected simulated retinal images.	23
5.3	Graphs comparing root-mean-square spherical aberration and PSNR/SSIM quality metrics for corrected and uncorrected simulated retinal images.	26

List of Tables

5.1	Settings used for model evaluation	16
5.2	Bunny images for varying coefficients of the vertical coma aberration	19
5.3	Bunny images for varying coefficients of the oblique trefoil aberration	22
5.4	Bunny images for varying coefficients of the spherical aberration	25

Acknowledgments

I would like to thank Professor Barsky for mentoring me through my four semesters in this group and encouraging me to explore uncharted territory. I am indebted to Joshua Chen, who has guided me through our research group's advances in compressive deconvolution. I would further like to acknowledge Matthew Fogel for assisting with data collection and debugging, as well as providing much needed documentation in our repositories to facilitate future research. I'd also like to mention, Siyu Zhang, who led me during my first semester on the vision correcting display project. Finally, I am extremely grateful to Professor Roorda for reviewing this work as a second reader.

Chapter 1

Background

1.1 Introduction

Over 1 billion people wear eyeglasses globally, [1] including the majority of adults in the United States [2]. These eyeglasses are vital in allowing them to see clearly, but there are several cases in which alternatives are preferable, such as contact lenses. Sometimes it is physically or aesthetically inconvenient to wear glasses [3]. Vision correcting displays do not require the user to wear anything; this device technology would allow users to see clearly in situations where glasses are not preferable: for example, while wearing virtual reality headsets; they are also adjustable per user, while modern corrective technology is prescribed for each user. This work delves into potential modifications for the vision correcting display for specific optical conditions and evaluates their effectiveness. This work builds upon the work and foundations of compressive deconvolution for the vision correcting display by Anmol Parande [4], further bridging the efficiency and quality trade-off.

1.2 The Eye

The anatomy of the eye is shown in Figure 1.1, taken from [5]. When light rays enter the eye, they are refracted by the **cornea** (the outermost layer of the eye). The cornea provides most of the refraction and has a fixed focusing power of 42 - 45 diopters. The light rays are then refracted further by the **lens** of the eye, which can vary in thickness and refractive power as the ciliary muscle contracts. They then pass through the vitreous cavity and activate photoreceptors that transmit electrical impulses to the brain. The layer of rod and cone photoreceptors comprising the **retina** resemble a matrix, and can be represented as an array in our simulation.

In perfect vision, each pixel of a screen refracts through the cornea and lens, activating corresponding photoreceptors so that the brain's reconstructed image is a clear representation of the screen. In Figure 1.2 taken from [6], the two light rays originating from the top of the tree travel in different directions, but they converge at a point on the retina. The retina is

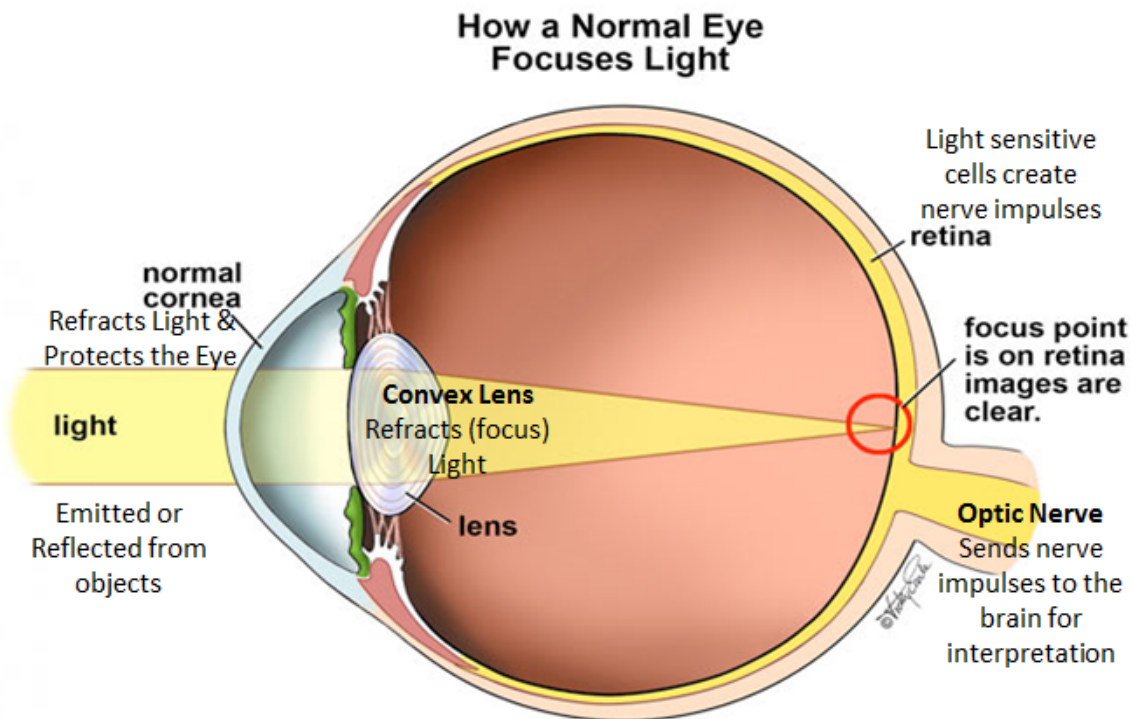


Figure 1.1: The eye focuses light through the cornea and lens onto the retina. The retinal image is transmitted to the brain through the optic nerve.

a certain distance from the lens, which is at the front of the eye. The relationship between the distance at which the light rays converge and the distance of the screen is dictated by the focal length, which is a function of the combined refractive power of the lens and cornea. Two quantities defining the range of vision are the near point and far point. The near point is the closest distance at which the eye can focus on an object, and is about 25 centimeters in adults with normal vision. The far point is the furthest distance at which the eye can focus on an object, and is usually infinite, as the ciliary muscle relaxes. Farsightedness occurs when the near point is further than normal. This work is most applicable to far sighted users, as they would benefit the most from vision correcting technology for hand held screens held close to the eyes.

The most common optical aberrations that require correction are defocus and astigmatism aberrations [7]. These are considered lower order aberrations of the eye and are rectifiable with corrective lenses. Higher order aberrations, or HOAs, are not treatable through traditional eyeglasses or soft contact lenses, and often require surgery. They can be caused by structural deformities, cataracts, or scarring, and tend to be too irregular for simple lenses to counteract. Higher order aberrations are not as common as lower order aberrations, and account for roughly 15% of all aberrations in the eye [8].

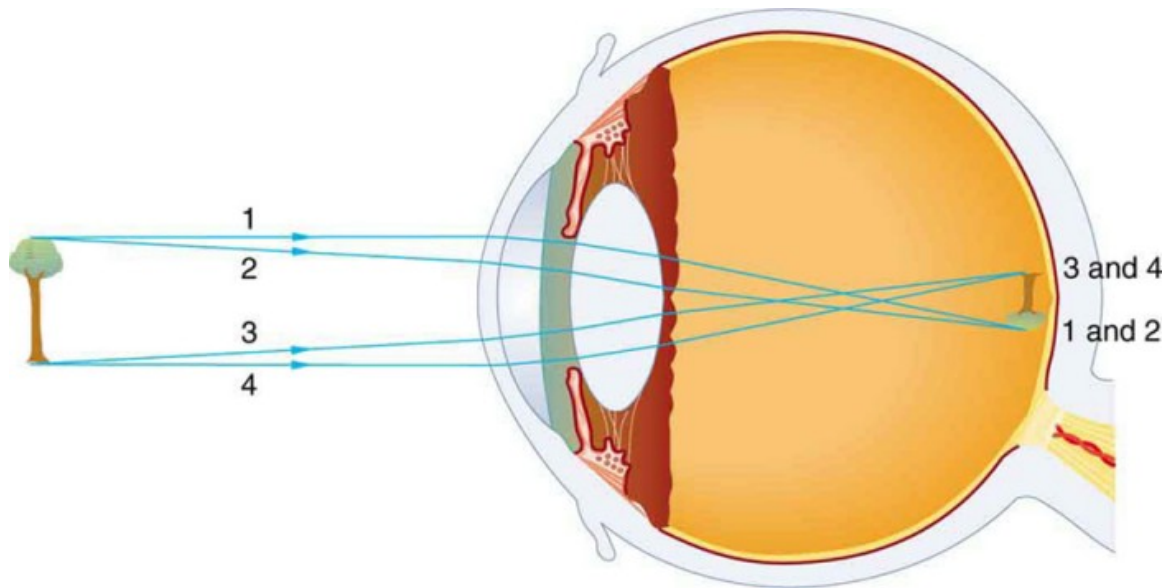


Figure 1.2: Multiple light rays originate from each point on the tree, are refracted by the lens, and converge on the retina.

1.3 Problem Statement

The problem guiding this research is the following:

Given the measurements and parameters of a user's optical system, can an image be displayed on some screen such that the user perceives a clear and in-focus image without the need of additional corrective technology?

The solution involves both new screen technology and performant algorithms to efficiently compute the images to be displayed. This work focuses on improving results for users with higher order aberrations. The experiments conducted to investigate these solutions use simulated conditions of presbyopia or hyperopia, since the targeted use cases of vision correcting displays are handheld devices, computers, and virtual reality headsets, all of which are affected by farsightedness.

Chapter 2

Related Work

2.1 VCD

Conventional screens display two dimensional arrays of pixels. Each pixel projects several light rays which refract through the cornea and lens of the eye and converge on the retina in the back of the eye. In perfect vision, each pixel on the screen maps to a “pixel” on the retina. However, in unfocused or misshapen eyes, the light rays emanating from a pixel do not converge perfectly on the retina due to improper refraction, leading to a blurry perception. This can be corrected through lenses that, along with the eye’s natural refractive capability, redirect light rays to converge crisply on the retina. The vision correcting display (VCD), takes a different approach to this problem. The VCD utilizes a parallax barrier to emit directional rays. These rays are pointed in such a way they will form a clear picture on the retina after refraction through the lens. In this work, the parallax barrier is implemented with a pinhole array mask.

2.2 Light Field Displays

Light field displays utilize multiple layers in order to simulate directional pixels. The first layer is a high-resolution 2D array of pixels, similar to a conventional screen. However, another layer of microlenses or **pinholes** are placed over the screen and this creates a many-to-one ratio of screen pixels to each pinhole, as seen in Figure 2.1 (taken from [9]). In this work, we use “screen” to refer to the high-resolution screen layer, “display” to refer to the light field display, and “sensor” to refer to the reconstructed retinal image. Light field displays already exist for simulating three dimensional space on a 2D screen as seen in Figure 2.2 (taken from [10]), but in this work they are repurposed for their quality of having directional rays, such that each display pixel has a different intensity in each direction.

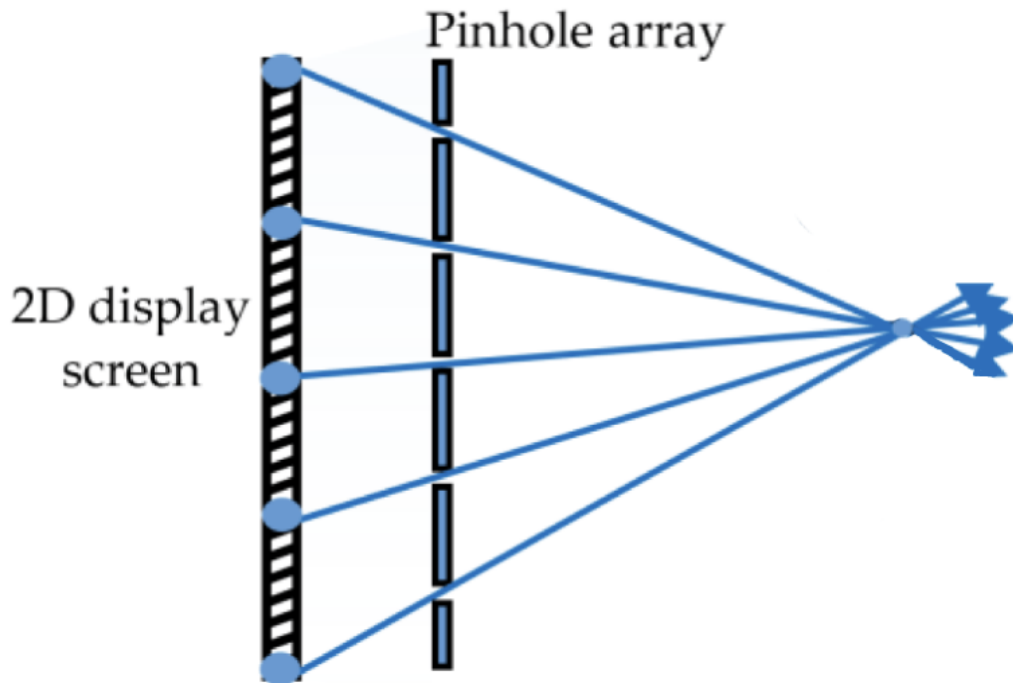


Figure 2.1: Pinhole arrays placed over pixel screens allow narrow, directional light rays to pass through.

2.3 Light Field Display Algorithms for Vision Correction

Ray Tracing Based Prefiltering Algorithms

A simpler method of reconstructing a screen image that will appear in-focus to the user is **ray tracing**. This method generates and simulates the movement of light rays from the screen, through the corresponding pinhole, through the cornea and lens, and onto the retina (sensor). There is a **one-to-one assumption** that each screen pixel can only be seen through one pinhole, which simplifies computation. The experiments in this work assume that the display is sufficiently distant from the aperture plane (the eye lens). The conditions for the one-to-one assumption are listed in [9]. The Ray tracing algorithms are generally not as effective as optimization based algorithms, but they are far faster, as there is no further optimization after the first iteration.

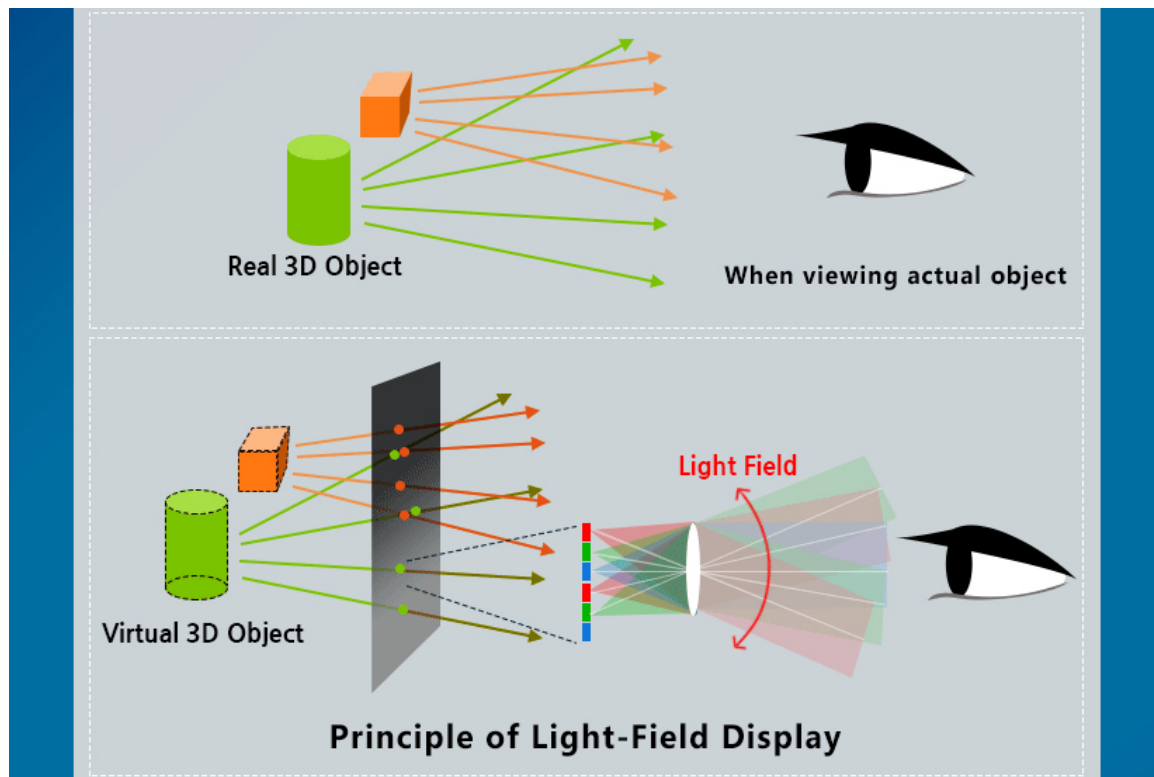


Figure 2.2: Light field displays can be used to create 3D effects by using directional light rays that simulate depth.

Point to Point, Many to Many, and Area to Area Algorithms

The **point-to-point** algorithm generates one ray from the center of each screen pixel to the nearest pinhole. The color of the screen pixel is determined from a weighted sum of pixels near where the ray intersects the retinal plane. That is, a screen pixel will be assigned to a bilinear interpolation of the four nearest pixels to the point u on the retinal plane.

The **area to area** algorithm generates two rays from the corners of the screen pixel and infers the area over which the entire screen pixel maps to the retina. It computes the screen pixel color as the integral of the color of the target image over the implied retinal pixels.

The **many-to-many** algorithm generates multiple rays from various positions within the screen pixel to the nearest pinhole. The screen pixel is then the average of all of the bilinear interpolations. The point-to-point algorithm is the many-to-many algorithm with one light ray sampled per screen pixel.

Optimization Based Algorithms

While ray tracing algorithms compute the value of screen pixels from sampling rays and interpolating colors, optimization based algorithms compute the relationship between the screen pixels and the resulting retinal pixels as a matrix, and then optimize screen pixels directly to achieve a retinal image as close to ideal. In this work, we will focus on using the Forward Optimization optimization-based algorithm to produce screen images that result in high quality simulated retinal images.

Forward Algorithm

In the Forward Algorithm, first introduced in [11], the Many to Many ray tracing algorithm is applied to form a matrix P that describes the relationship between the simulated retinal image \mathbf{y} and the screen image \mathbf{x} . The dimensions of P are the number of screen pixels times the number of retinal pixels. However, instead of bilinear interpolation, only the color of the nearest sensor pixel to the hit is recorded. The algorithm uses least squares to solve

$$\operatorname{argmin}_{\mathbf{x}} \|\mathbf{y} - P\mathbf{x}\|_2^2 \quad (2.1)$$

where \mathbf{y} is the target image. The least squares solution to this optimization problem is

$$\mathbf{x} = (P^T P)^{-1} P^T \mathbf{y} \quad (2.2)$$

however due to the huge size of the matrix, it is preferred to use an iterative solver such as the Limited-memory Broyden-Fletcher-Goldfarb-Shanno (LBFGS) algorithm [12]. The forward algorithm also requires the one-to-one assumption, which is valid for the experimental parameters used in this work.

Chapter 3

Compressed Sensing Approaches to Image Construction

The least squares optimization problem of solving for \mathbf{x} in (2.1) is infeasible at the size of the target images. For a 1280×720 pixel image with 921,600 pixels, if there were 5×5 screen pixels corresponding to each display pixel, the matrix storing the mapping from screen pixels to sensor pixels would have size $(1280 \times 720)^2 \times 5^2$, which is over 20 trillion parameters. If n is the number of sensor pixels per display pixel, and the size of the image is $w \times l$, then the size of the matrix would be $(wln)^2$, which is unfathomably large. The first workaround to this issue is a consequence of the one-to-one assumption, which reminds us that each screen pixel only has relevant rays (which project onto the retina) through one pinhole, and so the vast majority of the matrix is zero. In expectation, the number of nonzero entries in the matrix is roughly proportional to the number of screen pixels. We use a sparse format for storing this matrix in the code.

In this chapter, we will introduce the sampling problem, and under what conditions a discrete, time-varying signal can be perfectly reconstructed from a finite number of measurements. This is applicable to this work, as we work with 2D images flattened into 1D vectors. We will then expand sampling into "sensing," where the signal itself cannot be measured, but rather sensed through its projection onto another basis. The sensing approach represents reflects that the eye does not observe a perfect image, but rather the convolution of a perfect image with some blurring matrix. With enough sparsity in the signal, we can utilize compressed sensing to reconstruct the image, where the sensed measurements are of much lower dimension than the signal. We refer to the process of compressed sensing and reconstruction of the original image as **compressive deconvolution** [4].

3.1 Sampling Problem

Traditional sampling from a time varying signal $x(t)$ involves evaluating the function at time points $t_1, t_2 \dots t_n$ and inferring the function from those points. Let $t_k = Tk$. The extracted

signal is

$$y(t) = \sum_1^n x(t)\delta(t - t_k) = x(t) \sum_1^n \delta(t - Tk) \quad (3.1)$$

In this work, we represent 2D images as 1D flattened arrays. We treat images as signals that can be sampled at various pixels. While there is not as much significance of the signal itself, reconstructing the signal allows us to interpolate unknown points (other pixels). The Shannon Nyquist Theorem states that the sampling rate must be at least twice the highest frequency present within a signal for perfect reconstruction. However, this requirement can be further reduced in especially sparse signals through compressed sensing.

3.2 Compressed Sensing

Following the procedure from [13], [14], instead of directly sampling values of $x(t)$, we "sense" its projection onto the sensor ϕ_k through

$$y_k = \sum_{i=1}^n x(iT)\phi_k(iT) = \langle \mathbf{x}, \phi_k \rangle \quad (3.2)$$

where $\mathbf{x}, \phi \in \mathbb{R}^n$. A compressed measurement for \mathbf{x} across several points can be described as

$$\mathbf{y} = \Phi \mathbf{x} \quad (3.3)$$

where $\mathbf{y} \in \mathbb{R}^m$ and Φ is an $m \times n$ matrix. One condition for successful reconstruction of the signal is that it is sparse in some sparsifying basis Ψ , where Ψ is an $n \times n$ matrix. Most images are sparse in some wavelet basis. We can measure a signal's sparsity through the notion of S-sparsity, which means that it has at most S nonzero coordinates. Candes and Wakin derive this optimization problem in [13] as

$$\min_{\tilde{x} \in \mathbb{R}^n} \|\tilde{x}\|_{l_1} \quad \text{subject to} \quad y_k = \langle \phi_k, \Psi \tilde{x} \rangle \quad \forall k \in M \quad (3.4)$$

where M is a subset of size m of the n possible compressed measurements. In compressed sensing $m \ll n$. This can be condensed to

$$\min_{\tilde{x} \in \mathbb{R}^n} \|\tilde{x}\|_{l_1} \quad \text{subject to} \quad \mathbf{y} = \Phi \Psi \tilde{x} \quad (3.5)$$

We choose Φ , the sensing basis, so that it has low correlation with Ψ , the sparsifying basis. Then, information in measurements of Ψx will be spread out when multiplied by Φ , which helps create a well-conditioned least squares problem for image correction in this basis. We can use a structurally random matrix, introduced in [15]

$$\Phi = \sqrt{\frac{N}{M}} DFR \quad (3.6)$$

where R is a random $n \times n$ matrix, F is an orthonormal $n \times n$ matrix (such as the FFT matrix) and D samples m rows of FR . D is a subset of m rows of the identity matrix.

3.3 Compressive Deconvolution Objective

While the human eye sensor can only measure $H\mathbf{x}$, we can utilize compressive deconvolution in the following setup from [4]

$$\min_{\mathbf{x}} \frac{1}{2\mu} \|\Phi\mathbf{y} - \Phi H\mathbf{x}\|_2^2 + \gamma \|\Psi^{-1}H\mathbf{x}\|_1 \quad (3.7)$$

where \mathbf{y} is the ideal unblurred image, μ is a reconstruction error penalty hyperparameter, and γ is another hyperparameter that forces \mathbf{x} to be sparse in the wavelet basis. In practice, this optimization problem can be solved without computing these large matrices, and alternative computational representations or iterative optimizers that do not require the full, in-memory matrices still suffice. Parandé's work in [4] describes the ADMM (Alternating Method of Direct Multipliers) procedure to solve this problem.

Chapter 4

Simulating Higher Order Aberrations

Higher order aberrations are a class of optical aberrations that are not correctable by conventional lenses. Three of the more common higher order aberrations found in human eyes are coma, trefoil, and spherical aberrations. These correspond to radial orders 3 and 4 in Figure 4.1 taken from [16]. In this chapter, we will explain how rays are refracted through perfect lenses and how we represent light rays. Then, we will propose a fast method to simulate the refraction of light rays through an aberrated lens. Finally, we will introduce the wavefront aberration polynomial and Zernike Polynomials as a method of characterizing aberration profiles of eyes.

4.1 Ray-Tracing Model for Unaberrated Systems

Ray Representation

In this subsection, we will present a simplified model of the light transport introduced in Parande’s thesis [4]. We model the directional intensities of these light rays as a four dimensional scalar function $I(\mathbf{x}, \mathbf{u})$ from 2D point \mathbf{x} on the display plane to 2D point \mathbf{u} on the lens plane (where the eye refracts light). We specify the context of the intensity light ray intensity function where it changes. We will also model ray direction with the tuple $(\mathbf{x}, \mathbf{u}, \alpha, \beta)$ where α is the location of the start plane and β is the location of the end plane. We will define the optical axis as perpendicular to the start and end planes.

Ray Projection

We will use the following properties of light rays in this representation. We will define the optical axis as perpendicular to the planes containing the objects and the lens.

1. Translation along Optical Axis: The direction of the ray $(\mathbf{x}, \mathbf{u}, \alpha, \beta)$ is equivalent to the direction of the ray $(\mathbf{x}, \mathbf{u}, \alpha + \Delta, \beta + \Delta)$, where Δ is the length of translation along the optical axis.

2. Translation within Start Plane: The direction of the ray $(\mathbf{x}, \mathbf{u}, \alpha, \beta)$ is equivalent to the direction of the ray $(\mathbf{x} + \Delta, \mathbf{u} + \Delta, \alpha, \beta)$, where Δ is a 2D translation within the start plane.
3. Propagation of Ray: The direction of the ray $(\mathbf{0}, \mathbf{u}, 0, 1)$ is equivalent to the direction of the ray $(0, c\mathbf{u}, 0, c)$, where c is a scale factor of the distance between the start and end planes.

Thin Lens Equation

In this work, we use ray tracing to model the path of light rays through the optical system. When ray tracing through a constant focal length system, one way to compute the direction of the ray after refraction is to use the thin lens equation

$$\frac{1}{f} = \frac{1}{d_o} + \frac{1}{d_i} \quad (4.1)$$

1. This states that the incident rays of an object $1/d_o$ before a lens with focal length f converge to form an image at a distance $1/d_i$ behind the lens.
2. The 2D location of the image formed by the rays along the axes parallel to the orientation of the lens is that of the chief ray passing unrefracted through the center of the lens.
3. The direction of the rays after refracting through the lens is computed by subtracting the location of the image from the point where the ray enters the lens. The location of the image can be computed in 3D space using (1) and (2).

Wave Front Polynomial

However, for an aberrated system with a varying focal length over the surface of the lens, we use a hybrid approach between wavefront aberration and ray tracing. A **wavefront** is defined as the surface over which the phase of a wave is constant. The **optical path difference** (OPD) is the difference in path length between two rays (post refraction). The wavefront aberration is the path difference between the aberrated wave front and a spherical reference wavefront. These definitions are taken from [17]. We will denote the wavefront aberration as $W(x, y)$ or $W(\mathbf{x})$ if \mathbf{x} is 2D.

Our process for approximating the refraction of a ray through an aberrated lens is different from that of a perfect, spherical lens. Consistent with Figure 4.2 from [17], to model the passage of light through an eye, the ray will refract through the waveform from right to left. We begin by refracting the ray R_1 that starts at 2D location \mathbf{x} on the display plane and ends at 2D location on the aperture plane \mathbf{u} , $(\mathbf{x}, \mathbf{u}, \text{display}, \text{aperture})$, over the spherical, reference wavefront to obtain the ray $(\mathbf{u}, \mathbf{s}, \text{aperture}, \text{sensor})$. Note that $(\mathbf{u}, \mathbf{s}, \text{aberrated aperture}, \text{sensor})$ is the corresponding ray on the aberrated wavefront. We then create two

additional light rays with small translations of magnitude Δ within the aperture plane, and translate them forward along the optical axis by the wavefront aberration function magnitude evaluated at their respective coordinates. These three rays approximate the local curvature of the aberrated wavefront. The refracted ray is approximated as

$$\mathbf{w}_u = \left(\begin{bmatrix} \mathbf{u} + \begin{bmatrix} \Delta \\ 0 \end{bmatrix} \\ W \left(\mathbf{u} + \begin{bmatrix} \Delta \\ 0 \end{bmatrix} \right) \end{bmatrix} - \begin{bmatrix} \mathbf{u} \\ W(\mathbf{u}) \end{bmatrix} \right) \times \left(\begin{bmatrix} \mathbf{u} + \begin{bmatrix} 0 \\ \Delta \end{bmatrix} \\ W \left(\mathbf{u} + \begin{bmatrix} 0 \\ \Delta \end{bmatrix} \right) \end{bmatrix} - \begin{bmatrix} \mathbf{u} \\ W(\mathbf{u}) \end{bmatrix} \right) \quad (4.2)$$

where Δ is small. We use this cross product to find the normal vector to the aberrated wavefront near \mathbf{u} with direction \mathbf{w}_u , which allows us to compute \mathbf{s} . We are now able to trace light rays through aberrated optical systems and construct the H matrix for optimization based correction algorithms.

4.2 Zernike Polynomials

Zernike polynomials, first developed by Frits Zernike in 1934 [18], are useful for representing optical aberrations. Due to their polar representation, they easily scale, add, translate, and rotate. The Zernike polynomials also form an orthogonal set over the unit circle, allowing for unique decompositions of wavefronts into linear combinations of Zernike modes. Finally, certain Zernike modes model classical aberrations, such as comas, astigmatisms, and spherical aberrations [19]. Hence the Zernike basis is preferred for optical analysis.

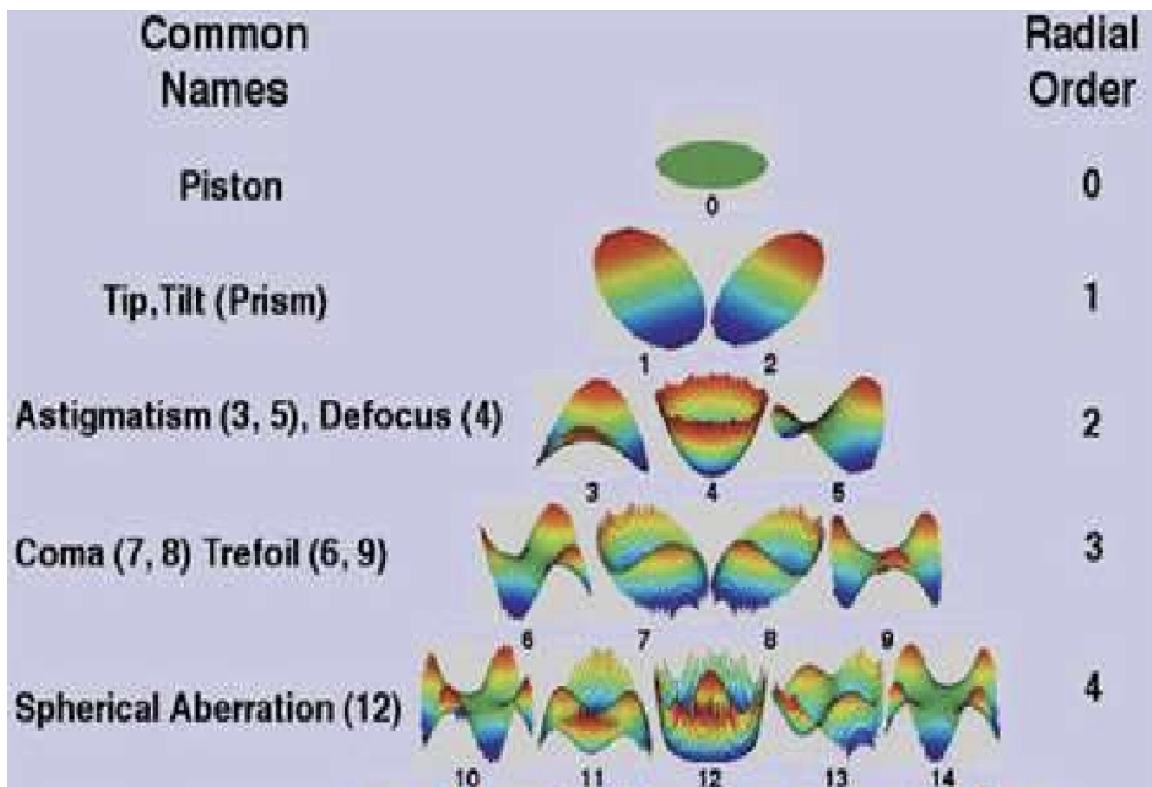


Figure 4.1: Zernike polynomials form a set of orthonormal waveforms that are useful for describing visual aberrations.

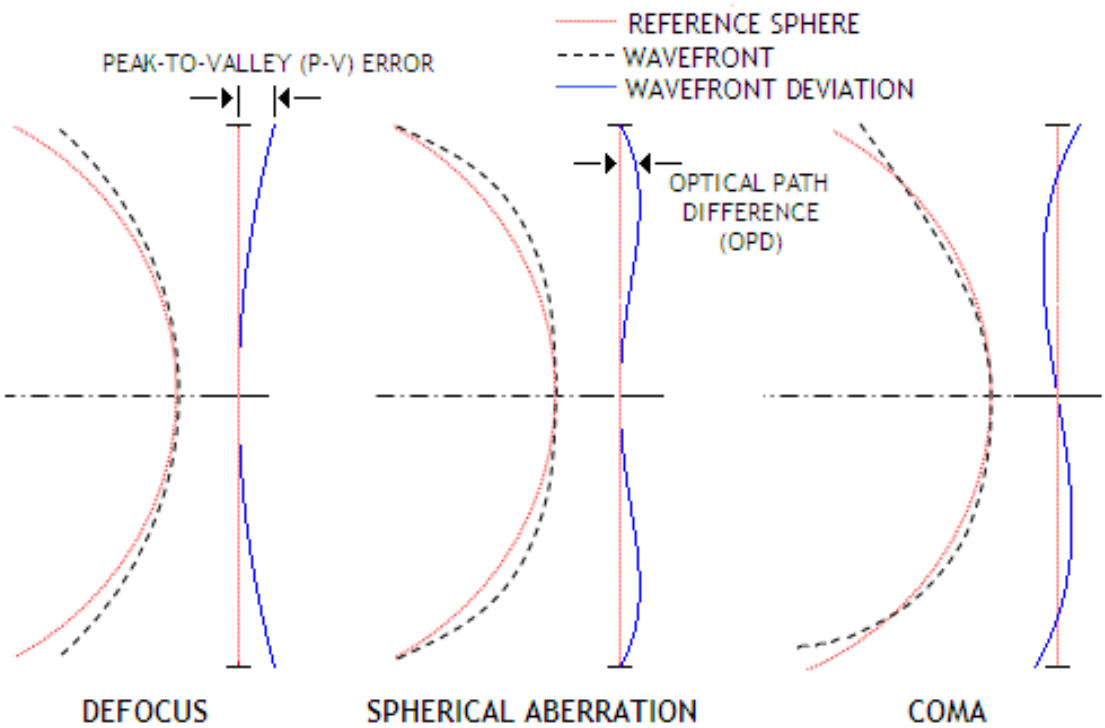


Figure 4.2: The wavefront aberration polynomial describes the optical path difference between the wavefront and an unaberrated, reference spherical wave front.

Chapter 5

Evaluation and Results

5.1 Display, User, and Model Parameters

The model used to evaluate the effects of higher order aberrations on vision correction is an optimization based compressive deconvolution prefilter. The sparse H matrix describing the relation between the screen pixels and retinal pixels is obtained through ray tracing. The data is collected with the following parameters in Table 5.1. To construct the H matrix, we will sample and trace 9 random rays originating from each screen pixel to the retina. The other parameters in the table include optimization penalty weights as well as specifications of the vision correcting display and the simulated optical system.

Parameter	Description	Value
μ	Reconstruction Penalty Weight	10^{-2}
γ	Sparsity Penalty Weight	10^{-3}
Viewing Distance	Distance to the observer's eye	300 mm
Near Point Distance	Distance from observer's eye to near focal plane	500 mm
Aperture Radius	Radius of aperture of observer's eye	1.5 mm
Focal Length	Focal Length of observer's optical system	20 mm
Ray Sampling	Number of times rays are sampled per screen pixel	9
Pinhole Mask Separation	Distance between pinhole array and underlying screen	6 mm
Screen Pixels per Pinhole	Screen Pixels per Pinhole	5×5
Sensor Pixel Pitch	Size of each screen pixel	0.078 mm

Table 5.1: Settings used for model evaluation

5.2 Aberration Parameters

This section discusses the experimental, varying parameters used for evaluating the effects of higher order aberrations on the simulated retinal image's visual quality. The eye lens is modeled as an aberrated wavefront in Figure 4.2, as a sum of a spherical wavefront and the wavefront aberration polynomial. We will model the effects where each wavefront aberration is a pure Zernike mode. We will model ranges of aberrations that are approximately found in the human eye.

Pure Zernike Aberrations

While we are focused on hyperopic (farsighted) vision and the correction of visual aberrations in nearby and handheld devices, we use statistics from [20] to determine appropriate testing ranges to represent in this work. In this study, 126 eyes from 63 subjects with age 26.4 ± 5.9 years were studied. The study used an aberrometer to record the wavefront of the participants' eyes. The study characterized the wavefront as a sum of a spherical, unaberrated wavefront and several weighted Zernike polynomials comprising the wavefront aberration.





The root mean square value range of the total aberration in the studied eyes were $6.85 \pm 2.4 \mu\text{m}$, which is approximately a 95% range of 0.002 to 0.011 mm amount of aberration. The range of measured coefficients for the vertical trefoil aberration, Z_3^{-3} , was 3×10^{-5} to 8×10^{-4} mm, or 3×10^{-2} to $8 \times 10^{-1} \mu\text{m}$.

5.3 Selected Images for Vertically Oriented Zernike Modes of Aberration

The prefilterings and projections in this section use a compression ratio of 0.3, so the sensing matrix Φ has an output to input dimension ratio of 0.3 (note that we represent images in 1D vectors). The three represented Zernike modes in this section are the vertical coma, oblique trefoil, and spherical aberration. These modes are shown in Figure 4.1 among radial orders 3 and 4. Zernike polynomials are denoted as Z_n^l , where n is the order of the polynomial and $0 \leq l \leq n$.

Vertical Coma Aberration Z_3^{-1}

The range of magnitudes of coma aberrations in [20] is 3×10^{-5} mm to 6×10^{-4} mm, or 3×10^{-2} μm to 6×10^{-1} μm . Each row of the table shows simulated retinal images of the optical system from Table 5.1 with the specified root-mean-square vertical coma aberration, with and without correction (prefiltering).

Parameter	Corrected Image	Parameter	Uncorrected Image
0 μm		0 μm	
0.1 μm		0.1 μm	
0.2 μm		0.2 μm	
0.3 μm		0.3 μm	
0.4 μm		0.4 μm	


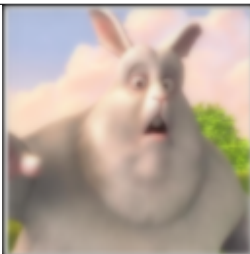

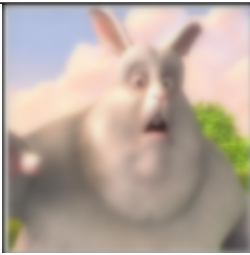

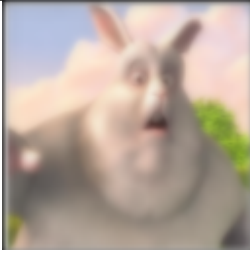
0.5 μm		0.5 μm	
0.6 μm		0.6 μm	
0.7 μm		0.7 μm	

Table 5.2: Bunny images for varying coefficients of the vertical coma aberration

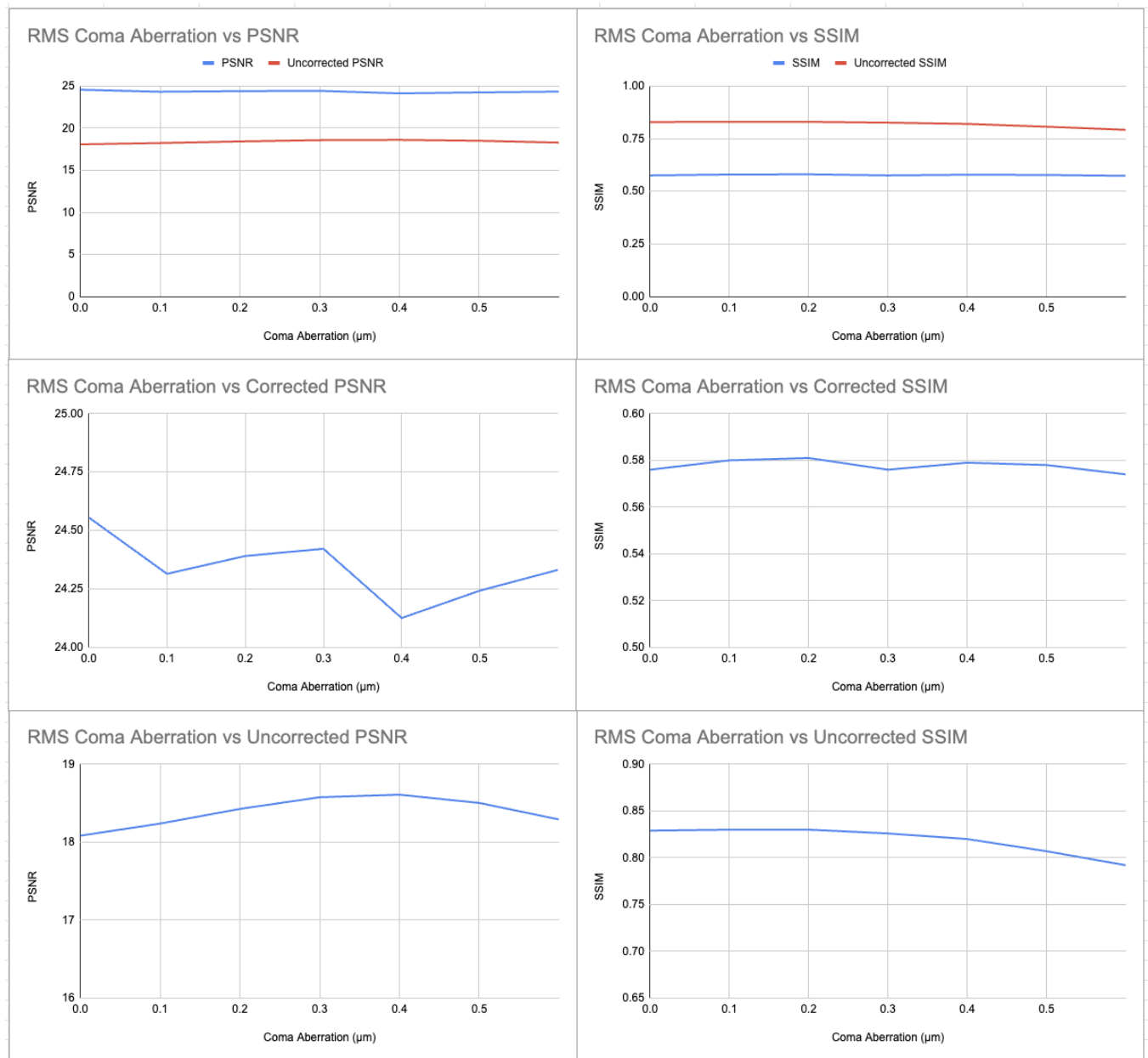




Figure 5.1: Graphs comparing root-mean-square coma aberration and PSNR/SSIM quality metrics for corrected and uncorrected simulated retinal images.

Oblique Trefoil Aberration Z_3^3

The range of magnitudes of trefoil aberrations in [20] is 3×10^{-5} mm to 8×10^{-4} mm, or 3×10^{-2} μm to 8×10^{-1} μm . Each row of the table shows simulated retinal images of the optical system from Table 5.1 with the specified root-mean-square oblique trefoil aberration, with and without correction (prefiltering).

Parameter	Corrected Image	Parameter	Uncorrected Image
0 μm		0 μm	
0.1 μm		0.1 μm	
0.2 μm		0.2 μm	
0.3 μm		0.3 μm	
0.4 μm		0.4 μm	


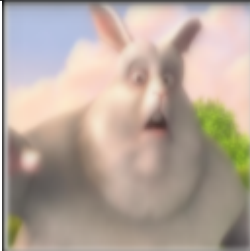



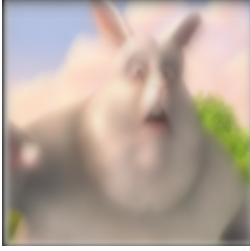

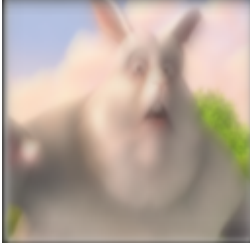
0.5 μm		0.5 μm	
0.6 μm		0.6 μm	
0.7 μm		0.7 μm	
0.8 μm		0.8 μm	

Table 5.3: Bunny images for varying coefficients of the oblique trefoil aberration

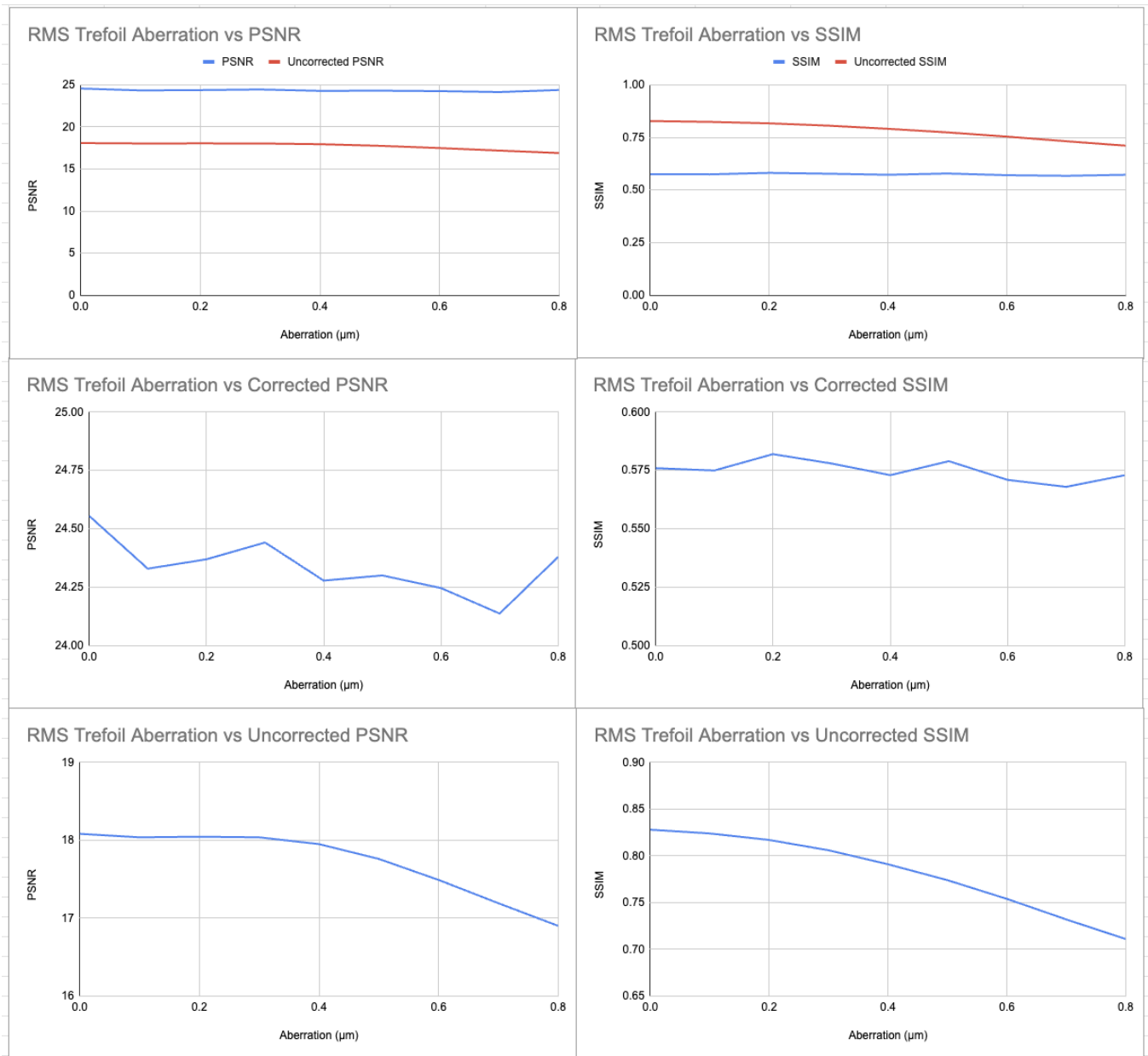


Figure 5.2: Graphs comparing root-mean-square trefoil aberration and PSNR/SSIM quality metrics for corrected and uncorrected simulated retinal images.

Spherical Aberration Z_4^0

The range of magnitudes of spherical aberrations in [20] is 0 mm to 4×10^{-4} mm, or $0 \mu\text{m}$ to $4 \times 10^{-1} \mu\text{m}$. Each row of the table shows simulated retinal images of the optical system from Table 5.1 with the specified root-mean-square spherical aberration, with and without correction (prefiltering).

Parameter	Corrected Image	Parameter	Uncorrected Image
$0 \mu\text{m}$		$0 \mu\text{m}$	
$0.1 \mu\text{m}$		$0.1 \mu\text{m}$	
$0.2 \mu\text{m}$		$0.2 \mu\text{m}$	
$0.3 \mu\text{m}$		$0.3 \mu\text{m}$	
$0.4 \mu\text{m}$		$0.4 \mu\text{m}$	

Table 5.4: Bunny images for varying coefficients of the spherical aberration

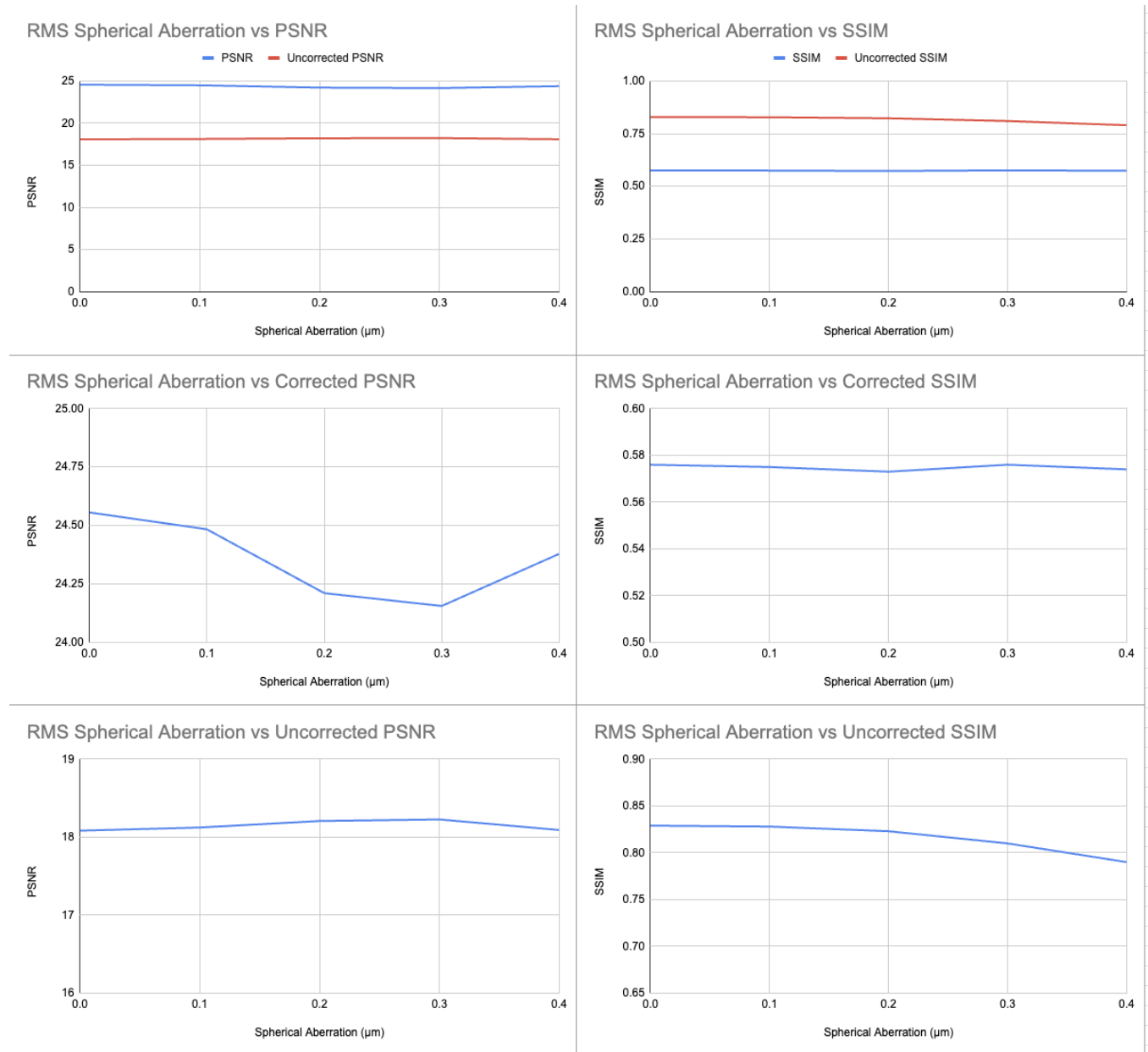


Figure 5.3: Graphs comparing root-mean-square spherical aberration and PSNR/SSIM quality metrics for corrected and uncorrected simulated retinal images.

5.4 Results

The vertical coma aberration was varied from $0 \mu\text{m}$ to $0.7 \mu\text{m}$ in Table 5.2, which is slightly beyond the range of RMS coma aberration observed in [20]. While the quality of the corrected, simulated images does not appear to decrease with increasing aberration magnitude, the uncorrected images significantly degrade in quality. In Figure 5.1, the PSNR (peak signal to noise ratio) of the corrected images is consistently higher than the PSNR of the uncorrected images. The changes in the PSNR of the corrected images across varying levels of aberration show no pattern, suggesting that the quality of the reconstruction is not determined by the aberration magnitude and the H matrix in this range. This is supported by the one-to-one assumption, as reasonable levels of aberration would map each retinal pixel to no more than one display pixel. The structural similarity (SSIM) metric paints a similar picture, but shows a degradation of quality of the simulated retinal images with increasing aberration.

Similar results were observed in the trefoil aberration experiment. The oblique trefoil aberration was varied from $0 \mu\text{m}$ to $0.8 \mu\text{m}$ in Table 5.3, as per the range of RMS trefoil aberration observed in [20]. The quality of the corrected, simulated images does not appear to decrease with increasing aberration magnitude. However, the uncorrected images significantly degrade in quality, noticeably above $0.4 \mu\text{m}$ of RMS aberration. In Figure 5.2, the PSNR (peak signal to noise ratio) of the corrected images is consistently higher than the PSNR of the uncorrected images. The changes in the PSNR of the corrected images across increasing levels of aberration stay within 0.5 PSNR points, but still seem to slightly degrade in quality, though imperceptibly. The structural similarity of the corrected images, though, seems to stay constant over the tested range, while the structural similarity of the uncorrected images significantly degrade.

The last of the experiments explored the quality of simulated retinal images of the optical system with spherical aberration. The RMS spherical aberration was varied from $0 \mu\text{m}$ to $0.4 \mu\text{m}$, which was approximately the range observed in [20]. Like in the other two experiments, the quality of the corrected and simulated images appears to be constant within the tested range, while the uncorrected images quickly degrade in quality. This is quite noticeable when the RMS aberration is at least $0.2 \mu\text{m}$. However the PSNR of the uncorrected simulated retinal images does not decrease with increasing RMS spherical aberration in Figure 5.3 which suggests the PSNR is not an appropriate metric for this measurement. The SSIM of the uncorrected simulated retinal images decreases with respect to RMS aberration above $0.2 \mu\text{m}$, which is in line with visual observations of Table 5.4.

Across all of the experiments, the SSIM of uncorrected simulated retinal images decreased with respect to the RMS aberration while the SSIM of corrected simulated retinal images stayed nearly constant. The SSIM metric corresponded better than PSNR to visual assessments of the quality of the images in Tables 5.2, 5.3, and 5.4.

Consistent with expectation, the measured quality of each uncorrected and simulated image is worse than that of the corresponding corrected and simulated image, including trials with $0 \mu\text{m}$ of higher order aberration. This is due to the hyperopic conditions of the

model (shown in Table 5.1) which introduces further blurring to each image.

This data suggests that within reasonable levels of aberration, compressive deconvolution based prefiltering can produce consistently satisfactory simulated retinal images.

Chapter 6

Future Work

This work extends optimization-based approaches to compressive deconvolution algorithms developed in [4] with support for modeling and handling higher order aberrations. While higher order aberrations with optically practical coefficients filter just as well as lower order aberrations, the optimization algorithms and framework used in this work are too slow to be useful for a visual device. As we are targeting efficient image correction and streaming capability, potential directions for further development include changes to the optimization problem solver and to the hardware it runs on. By loosening the criteria for optimization routine termination, there is a potential for large speedup at limited image quality cost. Exploring methods to parallelize the optimization routine will also improve the runtime, using an optimization routine with subproblems that can be run concurrently. Lastly, this work does not explore divide-and-conquer approaches to compressive deconvolution. This method allows compressive deconvolution to be run concurrently on pieces of the image with some reconciliation routine for the boundaries. If the size of the compressive deconvolution cell at least the size of the point spread region (the retinal area which can be reached by light rays originating from all the sensor pixels in the cell), the problem can be broken down and parallelized with low reconciliatory quality loss. This is a rich problem with potential for large speed-ups.

This work only uses two measures of image quality: PSNR and SSIM. There may be better metrics of image quality that can drive further insights about where the model's weak points are, and which types of aberrations or images are prone to significant quality reduction. Due to the sensing matrix sampling from the entire image at once, the greater point spread functions (lessened sparsity) that higher order aberrations introduced did not affect the optimal value of the objective. There were however, noticeable quality degradations on very high values of the trefoil aberration that were unaccounted for by these two metrics, which urges the usage of a more robust and representative image quality metric.

Chapter 7

Conclusion

This research delves into the impact of higher-order aberrations on vision correction, building upon existing frameworks for the optimization-based compressive deconvolution prefilter. Utilizing Zernike polynomials, which provide a comprehensive and orthonormal set of waveforms, the study models ray tracing through non-spherical waveforms to simulate and analyze their effects on visual quality. The model employs a sparse matrix, derived from ray tracing, to describe the relationship between screen pixels and retinal pixels. Key parameters, such as viewing distance, aperture radius, focal length, and others, were carefully selected to ensure realistic simulation conditions. The experimental setup included varying coefficients for vertical coma, oblique trefoil, and spherical aberrations, which were tested against a broad range of values within medically significant ranges.

The results indicate that within the practical range of aberration coefficients, the quality of the reconstructed and simulated retinal images remained stable, as evidenced by PSNR and SSIM metrics. This suggests that the compressive deconvolution prefilter is robust against higher-order aberrations within the studied range. However, the study did identify a perceptible degradation in image quality for higher coefficients of spherical aberrations, not captured by PSNR. This underscores the limitation of certain metrics in fully capturing the nuances of visual quality, particularly in the presence of complex aberrations. The ability for compressive deconvolution to successfully prefilter images is further limited by the one-to-one assumption, as the significant ray deviation for high-coefficient higher order aberrations may not obey this assumption.

The findings highlight the potential for optimization-based compressive deconvolution to effectively mitigate the effects of higher-order aberrations in practical applications, such as handheld devices and near-eye displays.

Bibliography

- [1] “Eyeglasses.” (2024), [Online]. Available: <https://my.clevelandclinic.org/health/treatments/eyeglasses>.
- [2] G. Sadosky. “Eyewear industry statistics and facts 2023.” (2023), [Online]. Available: <https://www.overnightglasses.com/eyewear-industry-statistics/>.
- [3] P. N.-C. Olivia J. Killeen Juno Cho, “Barriers and facilitators to obtaining eyeglasses for vulnerable patients in a michigan free clinic,” *Optom Vis Sci.*, 2022.
- [4] A. Parande, “Compressive deconvolution algorithms for a computational lightfield display for correcting visual aberrations,” M.S. thesis, EECS Department, University of California, Berkeley, May 2022. [Online]. Available: <http://www2.eecs.berkeley.edu/Pubs/TechRpts/2022/EECS-2022-110.html>.
- [5] *Human eye*. [Online]. Available: <http://science8sc.weebly.com/human-eye.html>.
- [6] “Physics of the eye.” (), [Online]. Available: <https://courses.lumenlearning.com/suny-physics/chapter/26-1-physics-of-the-eye/>.
- [7] W. D. Brad Kligman Brandon Baartman, “Errors in treatment of lower order aberrations and induction of higher order aberrations in laser refractive surgery,” *International Ophthalmology Clinics*, 2016.
- [8] “Higher-order aberrations.” (2019), [Online]. Available: <https://www.allaboutvision.com/conditions/aberrations.htm>.
- [9] S. P. e. a. Qiang Li Huan Deng, “A reflective augmented reality integral imaging 3d display by using a mirror-based pinhole array,” *Applied Sciences*, 2019.
- [10] “Light-field display.” (2021), [Online]. Available: <https://global.samsungdisplay.com/28567/>.
- [11] Z. Wu, “Investigating computational approaches and proposing hardware improvement to the vision correcting display,” M.S. thesis, EECS Department, University of California, Berkeley, May 2016. [Online]. Available: <http://www2.eecs.berkeley.edu/Pubs/TechRpts/2016/EECS-2016-67.html>.
- [12] J. N. Dong Liu, “On the limited memory bfgs method for large scale optimization,” *Mathematical Programming*, Aug. 1989.

- [13] E. J. Candes and M. B. Wakin, "An introduction to compressive sampling," *IEEE Signal Processing Magazine* 25.2, pp. 21–30, 2008.
- [14] A. B. Zhouye Chen and D. Kouam' e, "Compressive deconvolution in medical ultrasound imaging," *IEEE Transactions on Medical Imaging* 35.3, pp. 728–737, 2016.
- [15] T. T. D. et al., "Fast and efficient compressive sensing using structurally random matrices," *IEEE Transactions on Signal Processing* 60.1, pp. 139–154, 2012.
- [16] P. K. B. Koyuncu, "Simulation of corneal aberrations by using zernike polynomials," 2009.
- [17] "Wavefront aberration polynomial." (), [Online]. Available: https://www.montana.edu/jshaw/documents/8%20EELE582_S15_WavefrontAberrationFunction.pdf.
- [18] F. Zernike, "Beugungstheorie des schneidenverfahrens und seiner verbesserten form, der phasenkontrastmethode," *Physica*, vol. 1, no. 8, pp. 689–704, 1934.
- [19] C. T. Kuo Niu, "Zernike polynomials and their applications," *Journal of Optics*, 2022.
- [20] A. D. Farid Karimian Sepehr Feizi, "Higher-order aberrations in myopic eyes," *Journal of Ophthalmic & Vision Research*, 2010.